nature chemistry

ARTICLES

https://doi.org/10.1038/s41557-019-0246-5

N-heterocyclic carbene-functionalized magic-number gold nanoclusters

Mina R. Narouz[1], Kimberly M. Osten[2], Phillip J. Unsworth[1], Renee W. Y. Man[2], Kirsi Salorinne[2], Shinjiro Takano[3], Ryohei Tomihara[3], Sami Kaappa[4], Sami Malola[4], Cao-Thang Dinh[5], J. Daniel Padmos[1], Kennedy Ayoo[1], Patrick J. Garrett[1], Masakazu Nambo[2], J. Hugh Horton[1], Edward H. Sargent[5], Hannu Häkkinen[4*], Tatsuya Tsukuda[3,6*] and Cathleen M. Crudden[1,2*]

Magic-number gold nanoclusters are atomically precise nanomaterials that have enabled unprecedented insight into structure–property relationships in nanoscience. Thiolates are the most common ligand, binding to the cluster via a staple motif in which only central gold atoms are in the metallic state. The lack of other strongly bound ligands for nanoclusters with different bonding modes has been a significant limitation in the field. Here, we report a previously unknown ligand for gold(0) nanoclusters—N-heterocyclic carbenes (NHCs)—which feature a robust metal–carbon single bond and impart high stability to the corresponding gold cluster. The addition of a single NHC to gold nanoclusters results in significantly improved stability and catalytic properties in the electrocatalytic reduction of CO_2. By varying the conditions, nature and number of equivalents of the NHC, predominantly or exclusively monosubstituted NHC-functionalized clusters result. Clusters can also be obtained with up to five NHCs, as a mixture of species.

Magic-number gold nanoclusters stabilized by organic ligands are intriguing species that bridge the gap between molecules and materials[1–3]. Although clearly nanomaterials, with size-dependent properties, they can be described with a single molecular formula, have discrete electronic transitions due to their well-defined molecular orbitals and can be characterized by techniques usually employed in molecular science. Kornberg and colleagues' determination of the precise structure of the cluster $Au_{102}(SR)_{44}$ (SR = *p*-mercaptobenzoic acid) using single-crystal X-ray diffraction (XRD) was a watershed moment in understanding these nanomaterials[4]. The crystallographically determined structure partially confirmed earlier computational predictions on the bonding at the gold–thiolate interface and provided strong support for the 'superatom' theory of closed electronic shells, first described by Häkkinen and colleagues to explain why certain cluster sizes are over-represented among known species, and hence 'magic'[2,5].

Since the seminal paper by Kornberg, research into magic-number nanoclusters featuring different thiolates, metals, core configurations and applications has abounded[6–10]. However, with few exceptions, thiols and phosphines remain virtually the only organic ligands used to stabilize these structures (other than some work on alkynes)[11–17].

N-heterocyclic carbenes (NHCs) are phosphine analogues that have attracted considerable attention in organometallic chemistry and recently in surface science[18–31]. In organometallics, these ligands are known for their ability to form strong, substitutionally inert bonds to various metals[32,33]. Recently they have been shown to form highly robust self-assembled monolayers (SAMs) on Au(111) surfaces and nanoparticles[20,30]; however, their use as stabilizing ligands in magic-number nanoclusters has not been described previously. NHCs have, however been described as stabilizing ligands in small, mixed-valency clusters of three to four atoms in seminal works by the Corrigan[34,35], Sadighi[36] and Bertrand[37] groups.

Here, we report the first example of NHC-stabilized Au(0) nanoclusters. Au_{11} nanoclusters functionalized by up to five NHC ligands have been prepared and characterized. Remarkably, the addition of even one NHC to the Au_{11} cluster significantly increases the thermal stability of this important nanocluster and improves its activity in the electrochemical reduction of CO_2 to CO, which is a critically important reaction in the valorization of CO_2.

Results and discussion

Development of cluster synthesis. Our studies began with preformed phosphine-stabilized undecagold clusters $Au_{11}(PPh_3)_7Cl_3$ and $[Au_{11}(PPh_3)_8Cl_2]Cl$ (ref. [38]). Phosphine-stabilized clusters were chosen because NHC and phosphine ligands are both neutral and thus require no change in oxidation state or cluster charge to accompany an exchange reaction. Furthermore, phosphine-stabilized clusters do not have a layer of Au(I) atoms on the exterior, as is the case for thiolate-stabilized clusters. Treatment of $[Au_{11}(PPh_3)_8Cl_2]Cl$ (**2**) with di-isopropyl benzimidazolium hydrogen carbonate **1a**·H_2CO_3 (Fig. 1a) in THF at 66 °C gave predominantly a single NHC-containing cluster (**3a**, Table 1, entry 1). This cluster results from substitution of one phosphine ligand for the NHC (Fig. 1b). The less stable cluster $Au_{11}(PPh_3)_7Cl_3$ was not effective as a substitution partner.

Conclusive information about the cluster identity was obtained by mass spectrometry, which demonstrated that mono-substituted cluster **3a** is the predominant product, accompanied by small amounts of di-substituted cluster **4a** and starting material **2**

[1]Department of Chemistry, Queen's University, Kingston, Ontario, Canada. [2]Institute of Transformative Bio-Molecules (WPI-ITbM), Nagoya University, Nagoya, Japan. [3]Department of Chemistry, School of Science, The University of Tokyo, Bunkyo-ku, Tokyo, Japan. [4]Departments of Chemistry and Physics, Nanoscience Center, University of Jyväskylä, Jyväskylä, Finland. [5]Department of Electrical and Computer Engineering, The University of Toronto, Toronto, Ontario, Canada. [6]Elements Strategy Initiative for Catalysts and Batteries (ESICB), Kyoto University, Katsura, Kyoto, Japan.
*e-mail: hannu.j.hakkinen@jyu.fi; tsukuda@chem.s.u-tokyo.ac.jp; cruddenc@chem.queensu.ca

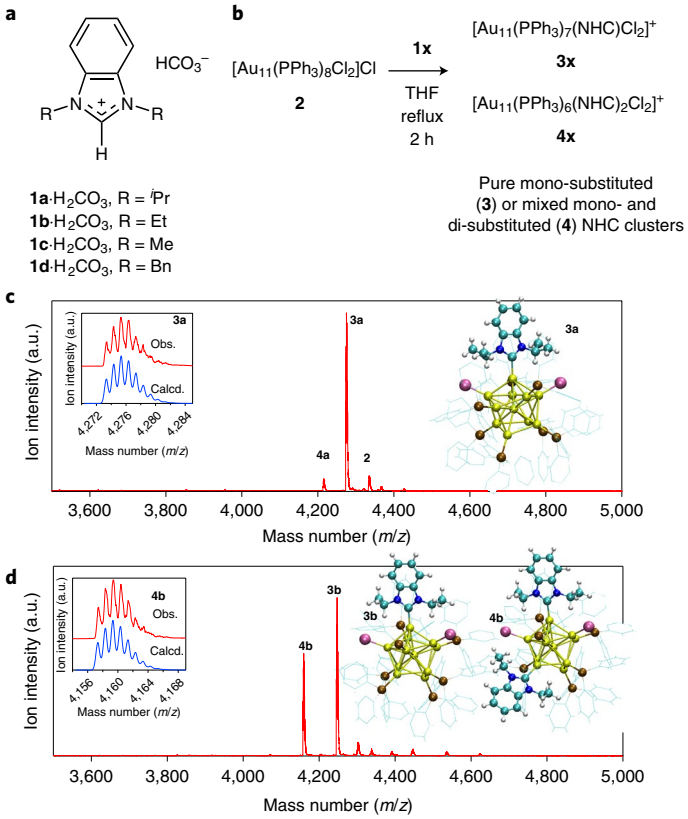

Fig. 1 | Synthesis and characterization of NHC-modified Au_{11} nanoclusters. **a**, Structure of NHC precursors employed in this study featuring a variety of organic substituents on the nitrogen atoms flanking the key carbon. **b**, Reaction of undecagold cluster $[Au_{11}(PPh_3)_8Cl_2]Cl$ (**2**) with NHC precursors from **a**, resulting in formation of new NHC-containing clusters. **c**, Mass spectrometric characterization of the reaction mixture leading to $[Au_{11}(PPh_3)_7(NHC^{i\text{-}Pr})Cl_2]Cl$ **3a**, along with the structure obtained by X-ray crystallography. Inset, observed versus calculated isotope pattern. The high level of purity is notable from the mass spectrum, which shows **3a** as the major product, along with small quantities of starting cluster **2** and di-substituted cluster $[Au_{11}(PPh_3)_6(NHC^{i\text{-}Pr})_2Cl_2]Cl$ **4a**. Colours in the atomistic structures: yellow, Au; purple, Cl; brown, P; blue, N, cyan, C; white, H. **d**, Mass spectrometric characterization of the reaction of **1b** with **2**, showing a mixture of **3b** and **4b** along with DFT-predicted structures. Note that the structure of **3a** shown in **c** is an actual crystal structure while **3b** and **4b** are DFT-simulated.

(Fig. 1c). Quantification of the cluster purity was accomplished by detailed ^{1}H NMR spectroscopic analysis. For precise details and replicate runs, see Supplementary Section 2. NHC nanoclusters were analysed before and after purification by chromatography on silica gel, which indicated that there was no change in the cluster distribution after chromatography and highlighted the stability of the cluster to chromatography (Supplementary Fig. 33). The main effect of purification was to remove molecular by-products such as $[Au(NHC)_2]^+$ and $OPPh_3$ (Supplementary Fig. 12).

Increasing the amount of **1a·H_2CO_3** to 5 equiv. resulted in larger amounts of the di-substituted cluster **4a**, with the addition of water attenuating reactivity and giving a more selective process (Table 1, entries 2 and 3). The use of the free NHC in place of the bicarbonate salt gave similar overall yields, but a mixture of clusters was obtained (entry 4). The mono-substituted cluster **3a** still predominated, but di-substituted cluster **4a** was observed along with tri-substituted cluster **5a**. ESI-MS (electrospray ionization mass spectrometry) revealed the presence of trace amounts of the tetra- and penta-substituted clusters **6a** and **7a**. Thus, the use of the bicarbonate salt **1a·H_2CO_3** at ~1 equiv. is important to produce clusters that are predominantly mono-substituted.

With conditions in hand for the preparation of NHC-stabilized clusters **3a** and **4a**, we then examined the effect of the NHC structure (Table 1). NHC precursors **1b–d·H_2CO_3** were used, where the nitrogen atoms of the NHC are substituted with Et, Me and Bn groups. Each of these relatively minor changes in NHC structure had an influence on the reaction. NHC precursor **1b·H_2CO_3** (R = Et) consistently gave a mixture of mono- and di-substituted clusters, regardless of the conditions or stoichiometry, suggesting that the initial substitution activates the cluster for a second displacement reaction (Fig. 1d and Table 1, entries 5—8). Again, increasing the amount of the NHC gave greater substitution (Supplementary Section 2).

NHC precursor **1c·H_2CO_3** (R = Me) behaved more like **1a·H_2CO_3** and allowed for the isolation of clean, mono-substituted cluster **3c** with no evidence for formation of the di-substituted cluster **4c** under optimized conditions. On average, lower isolated yields were observed in comparison to reactions with **1a·H_2CO_3** and **1b·H_2CO_3**, and the reaction was best run at lower temperatures (Table 1, entries 9 and 10). The addition of larger quantities of this small NHC gave cluster degradation rather than increased substitution (Supplementary Sections 2 and 3).

Finally, benzylated NHC precursor **1d·H_2CO_3** behaved similarly to **1b·H_2CO_3**, giving a mixture of mono-, di- and tri-substituted clusters **3d**, **4d** and **5d** even at 1.2 equiv. of the precursor. At higher loadings (9.0 equiv.), a mixture of clusters including mono- (**3d**), di- (**4d**), tri- (**5d**) and tetra- (**6d**) NHC-containing clusters was observed (Table 1, entries 11 and 12 and Supplementary Figs. 45–48).

Computational studies and structure prediction. Density functional theory (DFT, implemented as described in ref. [39]; for technical details see Supplementary Information) was used to investigate the energetics of substitution of the various phosphines in cluster **2** by NHCs (Fig. 2a). Introduction of NHC (**1a**) into cluster **2** was found to be thermodynamically favourable at most sites, with the exception of phosphine **8** (P8), which gave an unfavourable reaction energy change of +0.05 eV, probably due to steric constraints at this site (Fig. 2b). Introduction of the NHC by displacement of phosphines adjacent to the Au–Cl sites was uniformly preferred, with the single most favourable exchange predicted to occur at P2 for all NHCs examined. Differences between exchange at P2 and the next favourable phosphine energetically were 0.18 eV, 0.07 eV and 0.06 eV for **3a**, **3b** and **3c**, respectively (Fig. 2b and Supplementary Table 7). The calculated highest occupied molecular orbital–lowest unoccupied molecular orbital gaps for the mono-substituted clusters were largest for substitution at P2 for each NHC type, showing that the trends in electronic stability followed exchange energetics (Supplementary Table 8).

For the reaction of NHC precursor **1b·H_2CO_3** with **2** to form di-substituted clusters, the four lowest-energy isomers were found within a 0.1 eV window. Three of these included introduction of the NHC at P2 (Supplementary Table 9). NHC precursors **1a·H_2CO_3** and **1c·H_2CO_3** were also predicted to have favourable energetics for the production of di-substituted clusters. For example, substitution of **1a** and **1c** at P2 and P7 led to energy changes of −1.39 eV and −1.43 eV, respectively, suggesting that kinetic control rather than thermodynamics must play a role in the observation of predominantly or exclusively mono-substitution for these NHCs.

In the later stages of this work we were able to determine the atomistic structure of **3a** from a single-crystal X-ray analysis (vide infra). The crystal structure confirmed our DFT predictions that it is energetically optimal to replace phosphine P2 with an NHC in cluster **3a** (see the comparison of the predicted and observed structures in Supplementary Fig. 52). Three computational structure

Table 1 | Preparation of NHC-containing clusters by reaction of phosphine-containing cluster 2 with benzimidazolium hydrogen carbonates 1a–d

$[Au_{11}(PPh_3)_8Cl_2]^+ \xrightarrow[\text{Conditions}]{\textbf{1x}} [Au_{11}(PPh_3)_{8-n}(NHC)_nCl_2]^+$

Entry	1x·H_2CO_3 (equiv.)	Additive	Cluster(s) produced[a]	Yield[b] (%)
1	**1a** (1.2)	None	**3a**,**4a** (9:1)	22[c]
2	**1a** (5.0)	H_2O[d]	**3a**,**4a** (3:1)	26[c]
3	**1a** (5.0)	None	**3a**,**4a** (1:1)	38
4	**1a** (1.2)[e]	None	**3a**,**4a**,**5a** (2.6:1:1)	24
5	**1b** (1.2)	H_2O	**3b**,**4b** (2:1)	41
6	**1b** (1.2)	None	**3b**,**4b** (2:1)	20
7	**1b** (5.0)	H_2O	**3b**,**4b** (1:1)	64
8	**1b** (5.0)	None	**3b**,**4b** (1:1)	43
9	**1c** (1.2)	H_2O	**3c**	6[c]
10	**1c** (1.2)	H_2O[f]	**3c**	10[c]
11	**1d** (1.2)	None	**3d**,**4d**,**5d**[g]	18
12	**1d** (9.0)	None	**3d**,**4d**,**5d**,**6d**[g]	38

[a]Conditions: THF solvent, 66 °C, 2 h. **3x** clusters contain 1 NHC (n=1), **4x** (n=2), **5x** (n=3), **6x** (n=4), ratios determined by ^{1}H NMR spectroscopy, traces of starting cluster **2** present in some cases. [b]Isolated yields. [c]Average of 3–5 runs. [d]Water added at 500 ppm unless otherwise noted. [e]Free carbene employed. [f]40 °C, 1,000 ppm H_2O. [g]Exact ratios difficult to elucidate by NMR. Electrospray ionization mass spectrometry (ESI-MS) analysis shows decreasing amounts of more substituted clusters.

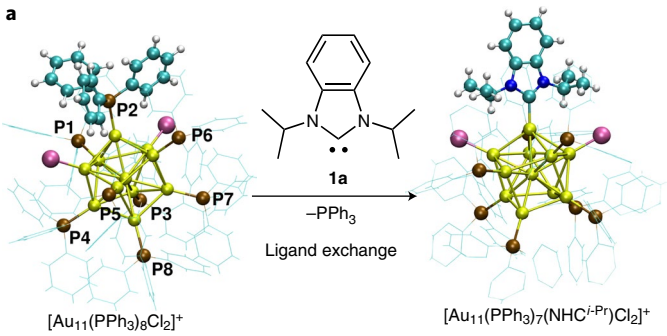

b

Phosphine	Energy (eV)[a]
P1	–0.64
P2	–0.93
P3	–0.73
P4	–0.55
P5	–0.41
P6	–0.40
P7	–0.75
P8	+0.05

[a]Changes in potential energy for reaction of **2** with **3a** by DFT.

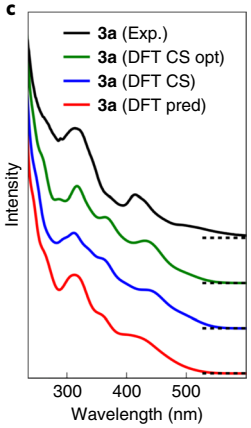

Fig. 2 | DFT and UV–vis spectroscopic prediction of structure for NHC-modified nanoclusters. a, Labelling of phosphines in $[Au_{11}(PPh_3)_8Cl_2]Cl$ (**2**) and exchange with **1a**. **b**, DFT-predicted changes in potential energy for reaction shown in **a** at each phosphine. **c**, Comparison of calculated optical spectra (red, blue, green curves) of cluster **3a** to experimental data (black). Three computed spectra are calculated for the initial DFT-predicted structure obtained by replacing phosphine P2 in cluster **2** by NHC **1a** (red), for the experimentally determined crystal structure (CS) (blue) and for DFT-optimization of the experimentally determined crystal structure (green). The computed spectra are blueshifted by 0.4 eV for better visual comparison to the experimental data.

models for **3a** were now in our hands: one based upon the structure predicted prior to obtaining an experimental crystal structure (red), one employing exact coordinates from the experimentally obtained crystal structure (blue) and one applying DFT optimization to the experimentally derived crystal structure (green).

The computed optical absorption spectra from these models are compared to the experimental data measured for **3a** in Fig. 2c. We notice that all computed spectra have spectral features that match the experimental data very well; however, the computed spectra systematically underestimate all transition energies by ~0.4 eV. This is understandable based on the properties of the DFT functional used in the calculation. The shift is corrected in Fig. 2c to enable a better visual comparison to experiment. The nature of the dominant two absorption features in the computed spectra (close to 300 nm and 450 nm in the shifted spectra) are further analysed in Supplementary Fig. 53. The dominant transitions were found to be either from Au *s*-type (450 nm) or Au *d*-type (300 nm) states to the empty states of the phenyl rings of the phosphines.

Spectroscopic characterization. The clusters were also extensively characterized by NMR spectroscopy, examining ^{1}H, ^{31}P and ^{13}C nuclei (Supplementary Section 3). The NHC carbon bound to Au could not be observed by ^{13}C NMR spectroscopy at natural abundance, but when cluster **3a** was prepared with ^{13}C enrichment at C2 of the NHC, the Au–C bond could be observed at 209 ppm. This signal appeared as an octet, indicating equivalent coupling to each of the seven phosphines (Fig. 3a). Because there are at least two unique environments for phosphines in any NHC-containing cluster, exchange processes must be happening on the timescale of the NMR experiment. ^{31}P NMR spectroscopy supports the presence of exchange phenomena at room temperature because a clean singlet was observed (Fig. 3b). To address this further, low-temperature ^{31}P NMR spectra were obtained for both **2** and **3a** (Supplementary Figs. 50 and 51). These spectra confirm the presence of an exchange phenomenon (or phenomena) on the NMR time scale. Interestingly, the NHC-functionalized cluster starts to show decoalescence at −10 °C, while the all-phosphine cluster **2** does not begin to decoalesce until close to −70 °C.

Information on the bonding and electronic properties of the clusters was also obtained through Au L_3-edge X-ray absorption spectroscopy (XAS). X-ray absorption near edge structure (XANES) spectra show a decrease in intensity when the NHC is introduced into the clusters (Supplementary Fig. 55), particularly for the Me derivative **3c**, which may be due to the electron-donating ability of NHCs[33,40,41].

Extended X-ray absorption fine structure (EXAFS) *R*-space spectra of the clusters revealed information on Au–C, Au–P and Au–Cl bonding, and Au–Au bonding within the cluster (Supplementary Fig. 54 and Supplementary Table 10). Analysis of Au–C bond lengths revealed that the Au–C(NHC) bond length in **3c** is 11.4 pm shorter than the corresponding Au–C bond in **3a**, consistent with steric differences between the NHC types. Most importantly, the introduction of NHC **1a** resulted in a 3 pm increase in the average Au–Au bond length for gold atoms on the exterior of the cluster relative to the all-phosphine cluster **2**, which suggests that NHC ligation leads to expansion of the outermost Au atoms in the cluster. A similar cluster expansion was not observed on ligation of the smaller NHC in cluster **3c**, which is interesting considering that this cluster has higher stability than **3a** (vide infra), suggesting an interplay between the experimental observations of cluster structure and stability.

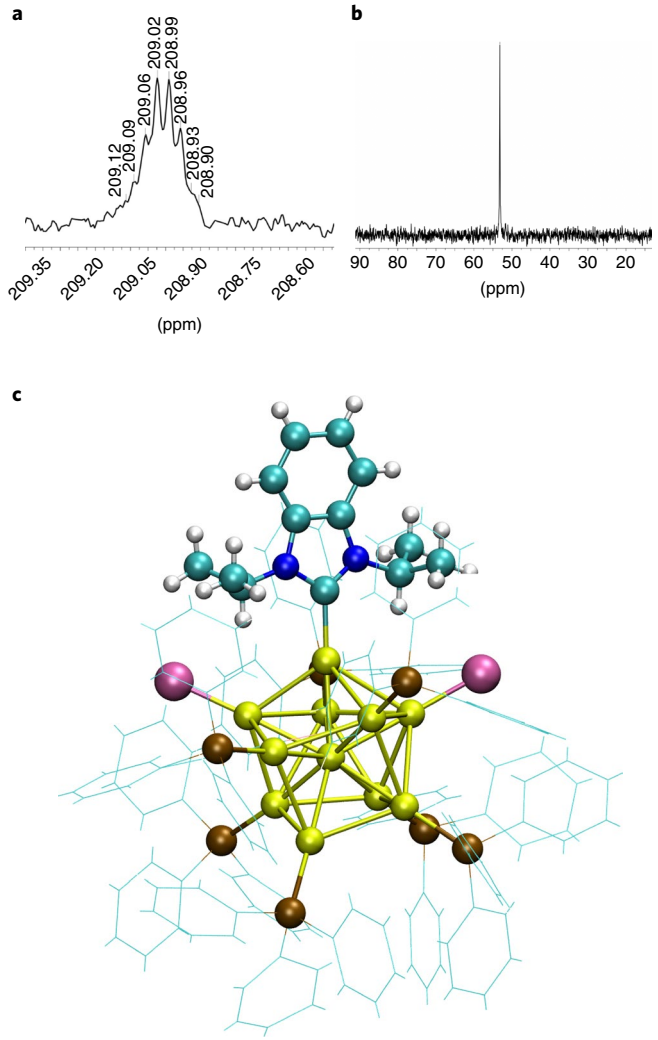

Fig. 3 | Spectroscopic and XRD characterization of NHC-substituted cluster 3a. a, ^{13}C {^{1}H} NMR spectrum of **3a** bearing ^{13}C-labelled NHC, which enables identification of the Au–C resonance. The signal appears as an octet from equal coupling to all seven phosphines. **b**, ^{31}P {^{1}H} NMR spectrum showing a single resonance at room temperature consistent with rapid exchange. **c**, Single-crystal XRD structure for NHC cluster **3a** showing NHC incorporation at P2 as proposed from DFT studies.

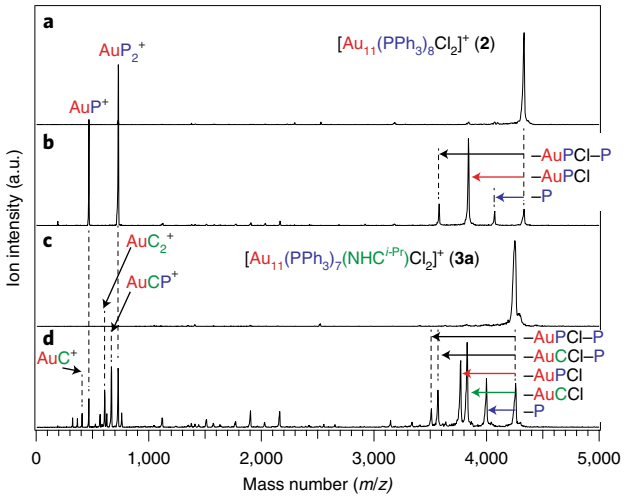

Fig. 4 | Assessment of stability and ligand dissociation by CID mass spectrometry. a, In-source CID mass spectra of cluster **2** recorded at the CID voltage of 0 V. Notations C and P represent $NHC^{i\text{-}Pr}$ and PPh_3, respectively. **b**, In-source CID mass spectra of cluster **2** recorded at 200 V. **c**, In-source CID mass spectra of cluster **3a** recorded at the CID voltage of 0 V. **d**, In-source CID mass spectra of cluster **3a** recorded at 200 V.

The longer Au–C bond and its effect on the underlying structure has precedent in prior DFT studies, which have proposed that binding of an NHC results in restructuring of the surface Au atoms in Au(111) systems[20,42,43]; however, this effect has been difficult to observe experimentally. The EXAFS results reported herein represent a direct measurement of the NHC influence on the underlying structure in metallic Au materials.

DFT calculations supported the trends observed experimentally by EXAFS. When the bond lengths were averaged over each of the optimized clusters, DFT studies predicted a 1.9 pm shorter Au–C bond in **3c** compared to **3a**. Similarly, the averaged calculated Au–Au bond length for the exterior gold atoms increased by 1.0 pm for cluster **3a** compared to **2**, while cluster **3c** showed no core expansion (within error).

Single-crystal XRD study of nanocluster 3a. X-ray quality single crystals of **3a** were grown by layering of *n*-hexane onto a solution of **3a** in dichloromethane at room temperature. After several days, reddish prisms of **3a** could be observed. Because dichloromethane co-crystallizes with **3a**, degradation of the crystal was observed on drying. The structure of the cluster obtained from this study was found to be the same as that predicted by DFT, resulting from displacement of P2 (Fig. 3c). Although static disorder in the region of the NHC ligand complicates a detailed analysis of the Au–C bond length, the value obtained (2.09(2) Å) is in the same range as that predicted by EXAFS analysis (2.161(6) Å, Supplementary Table 10). Taken in aggregate, the Au–Au bonds in the cluster were seen to contract upon introduction of the NHC ligand; however, localized bonds experience contractions and expansions that may be significant for catalysis (Supplementary Figs. 56 and 57 and Supplementary Tables 11 and 12).

Stability and catalytic activity of nanoclusters. Stability and ligand dissociation were also assessed using collision-induced dissociation mass spectrometry (CID-MS). In Fig. 4 we compare the in-source CID mass spectra of **2** and **3a**, recorded under identical conditions. Cluster **2** undergoes loss of $Au(PPh_3)Cl$ and PPh_3 as major CID paths (Fig. 4a). In contrast, loss of the $Au(NHC^{i\text{-}Pr})Cl$ unit was the most dominant CID pathway for **3a** (Fig. 4b), even though the ratio of $NHC^{i\text{-}Pr}$ to PPh_3 in the cluster is 1:7. In addition, direct dissociation of the $NHC^{i\text{-}Pr}$ ligand by Au–C bond cleavage was not observed under any conditions, in sharp contrast to **2**, where the loss of PPh_3 was observed. These results suggest that $NHC^{i\text{-}Pr}$ has significantly higher binding affinity to Au than PPh_3 does. These conclusions were supported by thermogravimetric analysis–mass spectrometry (TGA–MS) data, which also showed that phosphines are the first ligands to be lost (Supplementary Table 13 and Supplementary Figs. 61–64).

The thermal stability of the clusters was assessed by heating clusters in various solvents and monitoring the molecular transitions by UV–vis spectroscopy. The all-phosphine cluster **2** was used as a benchmark, which underwent complete decomposition after heating to 70 °C in pentanol (12 h) and toluene at 70 °C (24 h). By contrast, NHC-stabilized clusters showed dramatically improved stability, with **3c** displaying virtually no change over 24 h at 70 °C in toluene (Supplementary Fig. 58). Stability was reduced in the polar solvent pentanol, which allowed us to differentiate between the different NHC-functionalized clusters (Fig. 5a,b and Supplementary Fig. 59). Among the clusters examined, cluster stability tracked with sterics, with **3c** being the most stable, showing virtually no decomposition after 12 h at 70 °C in pentanol (Fig. 5a,b). Clusters **2**, **3a** and **3b**

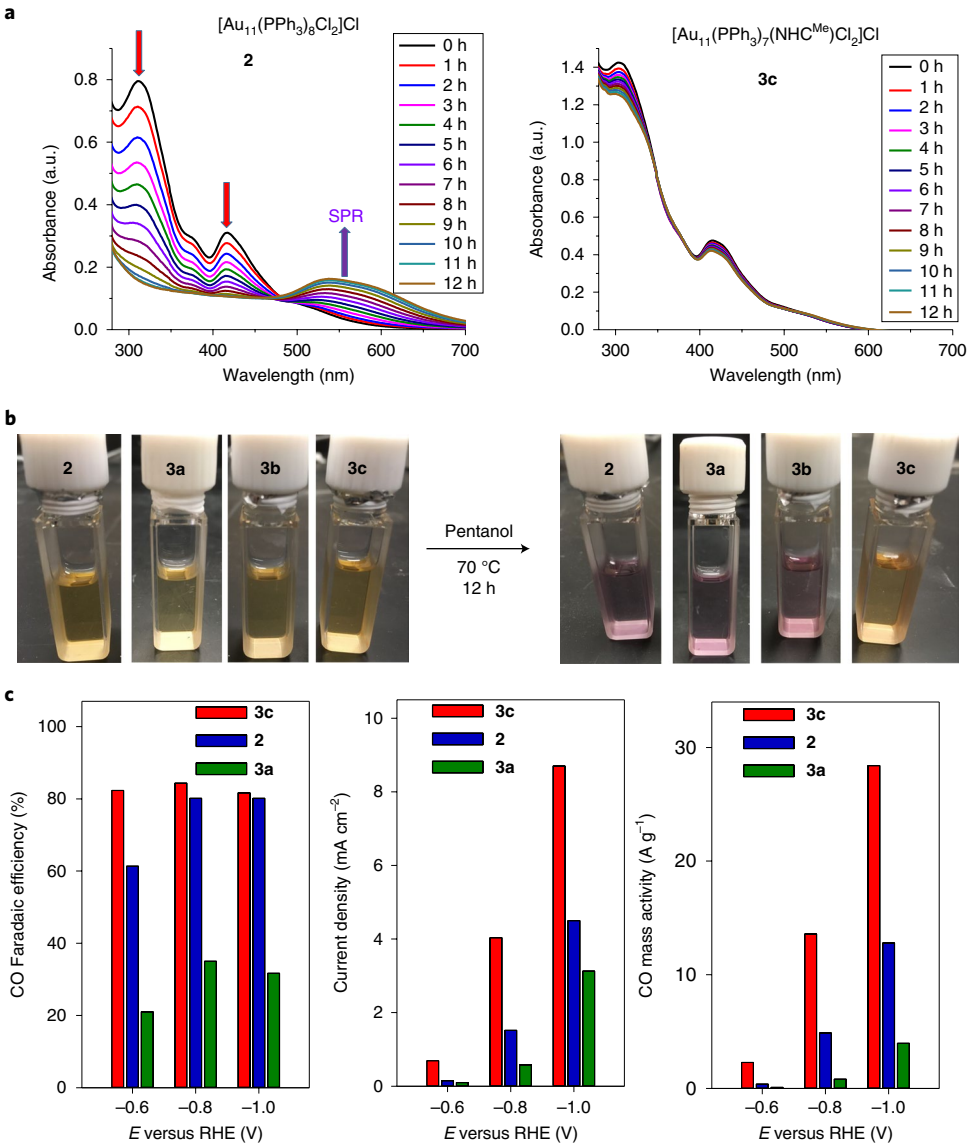

Fig. 5 | Nanocluster stability and activity in the electrocatalytic reduction of CO_2 to CO. a, UV–vis spectra of clusters **2** and **3c** in pentanol at 70 °C over 12 h. Cluster **2** decomposes to nanoparticles, evident by the loss of molecular signals at 405 and 310 nm and growth of the signal at 550 nm, while **3c** is completely stable. **b**, Nanoclusters **2**, **3a**, **3b** and **3c** before and after thermal treatment showing the decomposition of **2**, **3a** and **3b** while nanocluster **3c** remains intact. **c**, Catalytic activity and selectivity of nanoclusters **2**, **3a** and **3c** in the CO_2 to CO reduction showing that nanocluster **3c** has the highest Faradaic efficiency for CO, the highest current density and the highest mass activity among the nanoclusters tested. Although Faradaic efficiency seems independent of applied current, catalytic activity (as assessed through current density and mass activity) is highest at −1.0 V (versus reversible hydrogen electrode, RHE).

change colour from yellow (clusters) to purple (nanoparticles) after heating in pentanol (Fig. 5b). The relative stability of the clusters is thus **2** < **3a** < **3b** < **3c**. TGA–MS studies also showed that **3c** was the most stable of all clusters, with onset of ligand loss occurring 15–20 °C higher than all other clusters (Supplementary Figs. 60–64).

With a detailed understanding of structure and stability in hand, we examined these clusters as catalysts for the electrocatalytic reduction of CO_2 to CO (Fig. 5c)[44–49]. This is an important reaction because CO is the key component in many high-volume carbon–carbon bond-forming reactions such as the oxo reaction and the Cativa process.

Nanoclusters **2**, **3a** and **3c** were dissolved in a mixture of isopropanol and toluene (1:2 vol/vol) and deposited on carbon-paper electrodes with a catalyst loading of 0.25 mg cm^{-2}. The electrodes were then dried at room temperature before activating in air by heating to 180 °C for 2 h. This temperature was coincident with changes in the TGA-MS of the nanoclusters that are attributed to loss of a phosphine ligand (Supplementary Table 13 and Supplementary Figs. 61–64). Lower temperatures resulted in significantly lower activity, and longer treatment (6 h) at 180 °C was also detrimental (Supplementary Fig. 66).

Electroreduction of CO_2 was performed using a three-electrode system, with Ag/AgCl and Pt mesh used as reference and counter electrodes, which were submerged in a CO_2-saturated, 0.1 M $KHCO_3$ electrolyte solution. During the reaction, CO_2 was introduced by bubbling the gas through the electrolyte at 15 standard cubic centimetres per minute, and the product gases were analysed by gas chromatography.

As shown in Fig. 5c, nanocluster **3c** outperformed all-phosphine cluster **2** and cluster **3a** bearing an isopropylated NHC. Nanocluster

3c affected the electrocatalytic CO_2 reduction with the highest Faradaic efficiency (selectivity for CO production versus H_2). Similarly, cluster **3c** had the highest current density (mA cm^{-2}) and mass activity (A g^{-1}) of all clusters tested, at all voltages employed (Fig. 5c), with the greatest differences being observed at −1.0 V (versus RHE). Higher loadings of this nanocluster on the surface led to decreased performance, suggesting that more highly dispersed nanoclusters are more active than any agglomerated species that may form (Supplementary Fig. 67).

Compared with previously reported related NHC-functionalized nanoparticles, nanocluster **3c** displays similar levels of Faradaic efficiency and current density, although at more negative voltages[43,44]. The best nanostructured catalysts in the literature again give similar results, but at lower overpotentials, as a consequence of high catalyst loadings[43,47]. With the high mass activity already observed for **3c**, performance improvements would be expected through the use of higher-surface-area supports such as carbon nanoparticles[43].

To ensure that CO_2 is the source of the observed CO, the reaction was carried out with ^{13}C-labelled CO_2. Analysis of this reaction by gas chromatography–mass spectrometry (GC–MS) analysis (Supplementary Fig. 65) shows clear incorporation of the isotope into carbon monoxide (^{13}CO, $m/z=29$), confirming that the CO is produced from CO_2 by comparison with CO obtained from $^{12}CO_2$ where GC-MS analysis gave an m/z of 28 mass units for ^{12}CO. Only trace amounts of formate were observed after prolonged exposure (1%), illustrating the high selectivity of the reaction (Supplementary Fig. 68).

Interestingly, cluster **3c** is the only cluster of those examined that retained its structure and did not decompose to nanoparticles following extended thermal treatment. This observation leads to the intriguing possibility that having an intact nanocluster is important for catalytic activity, and illustrates the advantage of employing molecular species such as clusters as catalysts. It should be noted that NHC substitution does not uniformly lead to improved catalysts because cluster **3a** was outperformed by all-phosphine cluster **2**. Although the precise reasons for this difference are not presently clear, it may be that comparisons across cluster types are not as valid as comparisons within the NHC series **3a**, **3b** and **3c**. However, it is clear that the most stable cluster examined (**3c**) also gives the highest activity.

Conclusion

We have reported an example of the use of NHCs to stabilize gold(0) nanoclusters. The introduction of the NHC can be accomplished by a simple displacement reaction employing benzimidazolium hydrogen carbonate salts. The number of NHCs introduced is controllable by NHC structure, equivalents and reaction conditions. The structures of the NHC-containing clusters were predicted by DFT and confirmed by a combination of mass spectrometry, NMR, EXAFS, XANES, UV–vis spectroscopy and single-crystal XRD. The stability of the NHC-containing clusters was assessed by treatment at high temperature in a variety of solvents and by CID-MS and TGA–MS. NHC-containing clusters were found to be more stable than the all-phosphine clusters, with absolute stability dictated by the nature of the NHC. The performance of various clusters in electrocatalytic CO_2 reduction was found to correlate with cluster stability, with the most stable cluster having the highest Faradaic efficiency, catalytic activity and current density. These observations suggest that these novel NHC-stabilized gold clusters can have quantifiable benefits for electrocatalytic performance, which can be enhanced even further due to an atomically precise understanding of their structure.

Methods

In a two-neck flask equipped with a condenser and an argon balloon, a mixture of $[Au_{11}(PPh_3)_8Cl_2]Cl$ (**2**) and the corresponding benzimidazolium hydrogen carbonate (**1x**) were dissolved in THF (1 ml of THF per 1 mg of **2**). The resulting mixture was heated at 70 °C for 2 h before being cooled to room temperature. The solvent was removed in vacuo to give an orange solid, which was dissolved in dichloromethane (DCM) and passed through a Celite plug to remove any insoluble orange particles. The solvent was evaporated under an air stream or by rotary evaporator and the resulting orange solid was triturated with Et_2O (2 × 5 ml) to remove triphenylphosphine oxide. The resulting clusters were dissolved in a minimum amount of DCM to give a red solution, which was loaded onto a silica gel column packed with DCM/MeOH (25:1 vol/vol). The product was eluted with DCM/MeOH (9:1 v/v) to give the desired cluster as a red solid after solvent evaporation in vacuo. For details of specific experiments see Supplementary Information.

Data availability

Spectral and purity data are available for all new compounds, along with original NMR, MS, XPS, UV–vis, DFT, TGA–MS and electrochemical data. Single-crystal X-ray crystallographic data are included for cluster **3a**, while crystallographic data for cluster **3a** have been deposited at the Cambridge Crystallographic Data Centre under deposition no. CCDC 1878623. Copies of the data can be obtained free of charge via https://www.ccdc.cam.ac.uk/structures/. All other data supporting the findings of this study are available within the Article and its Supplementary Information, or from the corresponding author upon reasonable request.

Received: 6 April 2018; Accepted: 28 February 2019;
Published online: 15 April 2019

References

1. Bürgi, T. Properties of the gold–sulphur interface: from self-assembled monolayers to clusters. *Nanoscale* **7**, 15553–15567 (2015).
2. Häkkinen, H. The gold–sulfur interface at the nanoscale. *Nat. Chem.* **4**, 443–455 (2012).
3. Yamazoe, S., Koyasu, K. & Tsukuda, T. Nonscalable oxidation catalysis of gold clusters. *Acc. Chem. Res.* **47**, 816–824 (2014).
4. Jadzinsky, P. D., Calero, G., Ackerson, C. J., Bushnell, D. A. & Kornberg, R. D. Structure of a thiol monolayer-protected gold nanoparticle at 1.1 Å resolution. *Science* **318**, 430–433 (2007).
5. Häkkinen, H., Walter, M. & Grönbeck, H. Divide and protect: capping gold nanoclusters with molecular gold–thiolate rings. *J. Phys. Chem. B* **110**, 9927–9931 (2006).
6. Qian, H., Zhu, M., Wu, Z. & Jin, R. Quantum sized gold nanoclusters with atomic precision. *Acc. Chem. Res.* **45**, 1470–1479 (2012).
7. Hesari, M., Workentin, M. S. & Ding, Z. NIR electrochemiluminescence from Au_{25}^- nanoclusters facilitated by highly oxidizing and reducing co-reactant radicals. *Chem. Sci.* **5**, 3814–3822 (2014).
8. Jensen, K. M. Ø. et al. Polymorphism in magic-sized $Au_{144}(SR)_{60}$ clusters. *Nat. Commun.* **7**, 11859 (2016).
9. Chevrier, D. M., Yang, R., Chatt, A. & Zhang, P. Bonding properties of thiolate-protected gold nanoclusters and structural analogs from X-ray absorption spectroscopy. *Nanotechnol. Rev.* **4**, 193–206 (2015).
10. Chevrier, D. M., Zeng, C. J., Jin, R. C., Chatt, A. & Zhang, P. Role of Au_4 units on the electronic and bonding properties of $Au_{28}(SR)_{20}$ nanoclusters from X-ray spectroscopy. *J. Phys. Chem. C* **119**, 1217–1223 (2015).
11. Jin, R. Quantum sized, thiolate-protected gold nanoclusters. *Nanoscale* **2**, 343–362 (2010).
12. Tsukuda, T. & Häkkinen, H. *Protected Metal Clusters: From Fundamentals to Applications* (Elsevier, Amsterdam, 2015).
13. Wang, Y. et al. Atomically precise alkynyl-protected metal nanoclusters as a model catalyst: observation of promoting effect of surface ligands on catalysis by metal nanoparticles. *J. Am. Chem. Soc.* **138**, 3278–3281 (2016).
14. Wang, Y. et al. Site preference in multimetallic nanoclusters: incorporation of alkali metal ions or copper atoms into the alkynyl-protected body-centered cubic cluster $[Au_7Ag_8(C{\equiv}C^tBu)_{12}]^+$. *Angew. Chem. Int. Ed.* **55**, 15152–15156 (2016).
15. Wang, Y. et al. An intermetallic $Au_{24}Ag_{20}$ superatom nanocluster stabilized by labile ligands. *J. Am. Chem. Soc.* **137**, 4324–4327 (2015).
16. Wan, X. K., Tang, Q., Yuan, S. F., Jiang, D. E. & Wang, Q. M. Au_{19} nanocluster featuring a V-shaped alkynyl-gold motif. *J. Am. Chem. Soc.* **137**, 652–655 (2015).
17. Maity, P., Tsunoyama, H., Yamauchi, M., Xie, S. H. & Tsukuda, T. Organogold clusters protected by phenylacetylene. *J. Am. Chem. Soc.* **133**, 20123–20125 (2011).
18. Weidner, T. et al. NHC-based self-assembled monolayers on solid gold substrates. *Aust. J. Chem.* **64**, 1177–1179 (2011).
19. Zhukhovitskiy, A. V., Mavros, M. G., Voorhis, T. V. & Johnson, J. A. Addressable carbene anchors for gold surfaces. *J. Am. Chem. Soc.* **135**, 7418–7421 (2013).
20. Crudden, C. M. et al. Ultra stable self-assembled monolayers of N-heterocyclic carbenes on gold. *Nat. Chem.* **6**, 409–414 (2014).
21. Crudden, C. M. et al. Simple direct formation of self-assembled N-heterocyclic carbene monolayers on gold and their application in biosensing. *Nat. Commun.* **7**, 12654 (2016).

22. Zhukhovitskiy, A. V., MacLeod, M. J. & Johnson, J. A. Carbene ligands in surface chemistry: from stabilization of discrete elemental allotropes to modification of nanoscale and bulk substrates. *Chem. Rev.* **115**, 11503–11532 (2015).
23. Larrea, C. R. et al. N-heterocyclic carbene self-assembled monolayers on copper and gold: dramatic effect of wingtip groups on binding, orientation and assembly. *ChemPhysChem* **18**, 3536–3539 (2017).
24. MacLeod, M. J. & Johnson, J. A. Pegylated N-heterocyclic carbene anchors designed to stabilize gold nanoparticles in biologically relevant media. *J. Am. Chem. Soc.* **137**, 7974–7977 (2015).
25. Kim, H. K. et al. Reduction of the work function of gold by N-heterocyclic carbenes. *Chem. Mater.* **29**, 3403–3411 (2017).
26. Wang, G. et al. Ballbot-type motion of N-heterocyclic carbenes on gold surfaces. *Nat. Chem.* **9**, 152–156 (2016).
27. Engel, S., Fritz, E. C. & Ravoo, B. J. New trends in the functionalization of metallic gold: from organosulfur ligands to N-heterocyclic carbenes. *Chem. Soc. Rev.* **46**, 2057–2075 (2017).
28. Moller, N. et al. Stabilization of high oxidation state upconversion nanoparticles by N-heterocyclic carbenes. *Angew. Chem. Int. Ed.* **56**, 4356–4360 (2017).
29. Salorinne, K. et al. Water-soluble N-heterocyclic carbene-protected gold nanoparticles: size-controlled synthesis, stability and optical properties. *Angew. Chem. Int. Ed.* **56**, 6198–6202 (2017).
30. Man, R. W. Y. et al. Ultrastable gold nanoparticles modified by bidentate N-heterocyclic carbene ligands. *J. Am. Chem. Soc.* **140**, 1576–1579 (2018).
31. Rühling, A. et al. Modular bidentate hybrid NHC–thioether ligands for the stabilization of palladium nanoparticles in various solvents. *Angew. Chem. Int. Ed.* **55**, 5856–5860 (2016).
32. Crudden, C. M. & Allen, D. A. Stability and reactivity of N-heterocyclic carbene complexes. *Coord. Chem. Rev.* **248**, 2247–2273 (2004).
33. Hopkinson, M. N., Richter, C., Schedler, M. & Glorius, F. An overview of N-heterocyclic carbenes. *Nature* **510**, 485–496 (2014).
34. Polgar, A. M., Weigend, F., Zhang, A., Stillman, M. J. & Corrigan, J. F. A N-heterocyclic carbene-stabilized coinage metal–chalcogenide framework with tunable optical properties. *J. Am. Chem. Soc.* **139**, 14045–14048 (2017).
35. Azizpoor Fard, M., Levchenko, T. I., Cadogan, C., Humenny, W. J. & Corrigan, J. F. Stable -ESiMe$_3$ complexes of Cu^{I} and Ag^{I} (E=S, Se) with NHCs: synthons in ternary nanocluster assembly. *Chem. Eur. J* **22**, 4543–4550 (2016).
36. Robilotto, T. J., Bacsa, J., Gray, T. G. & Sadighi, J. P. Synthesis of a trigold monocation: an isolobal analogue of $[H_3]^+$. *Angew. Chem. Int. Ed.* **51**, 12077–12080 (2012).
37. Jin, L. et al. Trinuclear gold clusters supported by cyclic (alkyl)(amino) carbene ligands: mimics for gold heterogeneous catalysts. *Angew. Chem. Int. Ed.* **53**, 9059–9063 (2014).
38. McKenzie, L. C., Zaikova, T. O. & Hutchison, J. E. Structurally similar triphenylphosphine-stabilized undecagolds, $Au_{11}(PPh_3)_7Cl_3$ and $[Au_{11}(PPh_3)_8Cl_2]Cl$, exhibit distinct ligand exchange pathways with glutathione. *J. Am. Chem. Soc.* **136**, 13426–13435 (2014).
39. Enkovaara, J. et al. Electronic structure calculations with GPAW: a real-space implementation of the projector augmented-wave method. *J. Phys. Condens. Matter* **22**, 253202 (2010).
40. Zhang, P. & Sham, T. K. X-ray studies of the structure and electronic behavior of alkanethiolate-capped gold nanoparticles: the interplay of size and surface effects. *Phys. Rev. Lett.* **90**, 245502 (2003).
41. Lopez-Cartes, C. et al. Gold nanoparticles with different capping systems: an electronic and structural XAS analysis. *J. Phys. Chem. B* **109**, 8761–8766 (2005).
42. Tang, Q. & Jiang, D.-E. Comprehensive view of the ligand–gold interface from first principles. *Chem. Mater.* **29**, 6908–6915 (2017).
43. Rodríguez-Castillo, M. et al. Reactivity of gold nanoparticles towards N-heterocyclic carbenes. *Dalton Trans.* **43**, 5978–5982 (2014).
44. Tang, Q. et al. Lattice-hydride mechanism in electrocatalytic CO_2 reduction by structurally precise copper-hydride nanoclusters. *J. Am. Chem. Soc.* **139**, 9728–9736 (2017).
45. Cao, Z. et al. A molecular surface functionalization approach to tuning nanoparticle electrocatalysts for carbon dioxide reduction. *J. Am. Chem. Soc.* **138**, 8120–8125 (2016).
46. Cao, Z. et al. Chelating N-heterocyclic carbene ligands enable tuning of electrocatalytic CO_2 reduction to formate and carbon monoxide: surface organometallic chemistry. *Angew. Chem. Int. Ed.* **57**, 4981–4985 (2018).
47. Gray, H. B. Powering the planet with solar fuel. *Nat. Chem.* **1**, 7 (2009).
48. Liu, M. et al. Enhanced electrocatalytic CO_2 reduction via field-induced reagent concentration. *Nature* **537**, 382–386 (2016).
49. Zhang, L., Zhao, Z.-J. & Gong, J. Nanostructured materials for heterogeneous electrocatalytic CO_2 reduction and their related reaction mechanisms. *Angew. Chem. Int. Ed.* **56**, 11326–11353 (2017).

Acknowledgements

C.M.C., J.H.H. and E.H.S. acknowledge support from the Natural Sciences and Engineering Research Council of Canada (NSERC) and the Canada Foundation for Innovation (CFI) and the Ministry of Research Innovation (MRI) in terms of discovery grants and infrastructure grants, respectively. K.A. and P.J.G. thank NSERC for support through the awarding of USRA fellowships. M.R.N. thanks the Ontario Graduate Scholarship programme and Queen's University for fellowship support. This work was supported by KAKENHI from the Japan Society for the Promotion of Science (JSPS; 17H03030 and 16K13962 to C.M.C. and 17H01182 to T.T.), Nanotechnology Platform (project no. 12024046) and the Elements Strategy Initiative for Catalysts & Batteries (ESICB). J.S.P.S. and N.U. acknowledge funding of this research through The World Premier International Research Center Initiative (WPI) programme. The computational work was supported by the Academy of Finland through the Academy Professorship of H.H. All computations were carried out at the Finnish CSC computer centre. S.K. thanks the Väisälä Foundation for a personal PhD study grant. K. Itami is thanked for assistance with the preparation of this manuscript.

Author contributions

C.M.C., P.J.U., M.R.N. and K.S. designed and carried out the synthesis of the nanoclusters, assisted by K.A., P.J.G., M.N., K.M.O. and R.W.Y.M. K.M.O. and R.W.Y.M. optimized the synthetic procedures and purifications and acquired TGA–MS data. MS analysis was performed and interpreted by S.T., R.T. and T.T., including CID MS. Crystallization of **3a** was carried out by M.N. and S.T. on a sample prepared and purified by K.M.O. DFT studies, including prediction of structure and optical spectra, were carried out by S.K., S.M. and H.H. EXAFS and XANES studies were carried out and interpreted by J.H.H. and J.D.P. Electrocatalytic studies were performed and interpreted by C.-T.D. and E.H.S. The manuscript was written by C.M.C. with assistance from co-authors.

Competing interests

The authors declare no competing interests.

Additional information

Supplementary information is available for this paper at https://doi.org/10.1038/s41557-019-0246-5.

Reprints and permissions information is available at www.nature.com/reprints.

Correspondence and requests for materials should be addressed to H.H., T.T. or C.M.C.

Publisher's note: Springer Nature remains neutral with regard to jurisdictional claims in published maps and institutional affiliations.